UNIVERSITY OF CALIFORNIA SAN DIEGO

Regionalized differences in cardiomyocyte cytoskeletal organization during chamber curvature morphogenesis

A Thesis submitted in partial satisfaction of the requirements
for the degree Master of Science

in

Biology

by

Gabriel Avillion

Committee in charge:

Professor Deborah Yelon, Chair
Professor Xin Sun
Professor David Traver

2022

The Thesis of Gabriel Avillion is approved, and it is acceptable in quality and form for publication on microfilm and electronically.

University of California San Diego

2022

DEDICATION

I dedicate this thesis to my mother, Kate Barron-Avillion, and my father, Ron Avillion.

TABLE OF CONTENTS

LIST OF FIGURES

LIST OF ABBREVIATIONS

OC	outer curvature
IC	inner curvature
WT	wild-type
LHT	linear heart tube
OFT	outflow tract
AVC	atrioventricular canal
HPF	hours post fertilization
p-Myo	phosphorylated myosin
Cdh2	N-cadherin
F-actin	filamentous actin
Alcama	activated leukocyte cell adhesion molecule a

ACKNOWLEDGEMENTS

Figure 1 contains material adapted from Auman et al., 2007 as well as unpublished work by Dena M. Leerberg. Figure 2 contains unpublished material coauthored with Dena M. Leerberg.

VITA

2021 Bachelor of Science in Biochemistry and Cell Biology, University of California San Diego

2022 Master of Science in Biology, University of California San Diego

ABSTRACT OF THE THESIS

Regionalized differences in cardiomyocyte cytoskeletal organization during chamber curvature morphogenesis

by

Gabriel Avillion

Master of Science in Biology

University of California San Diego, 2022

Professor Deborah Yelon, Chair

Development of the vertebrate heart involves the collaboration between an array of different cell types, each engaging in a meticulously coordinated symphony of spatially and temporally regulated morphogenetic behaviors. Even small errors in cardiac morphogenesis can have severe physiological consequences. In an effort to understand the regulators of cardiac morphogenesis, prior studies have examined the regionalized changes in cell morphology accompany chamber curvature formation. However, we do not yet fully

understand the subcellular mechanisms that drive these cell shape changes. Prior studies have also indicated that actomyosin dynamics are important for chamber curvature morphogenesis, and multiple groups have observed differential organization of F-actin in cardiomyocytes of the inner and outer chamber curvatures. Here, we aimed to develop a comprehensive approach to identify distinctions between the actomyosin organization in inner and outer curvature cardiomyocytes that might promote regional changes in cell morphologies. We show that the actomyosin network indeed exhibits differential patterns of organization between cardiomyocytes in the inner and outer ventricular curvatures. We also find that *tbx5a* mutants, which fail to undergo proper curvature formation, fail to develop curvature-specific patterns of subcellular actomyosin organization. From these data, we propose a model in which the acquisition of regionalized actomyosin organization patterns drives curvature formation by promoting the development of curvature-specific cell morphologies.

INTRODUCTION

Organogenesis involves the precise coordination of numerous cellular behaviors to produce a functional organ. Cell growth and division enable organ growth, while behaviors like movement and shape change often mediate transitions in organ morphology (Eder et al., 2017; Heisenberg & Bellaïche, 2013). The heart is a fascinating example of organogenesis, where multiple cell types coordinate several of the aforementioned behaviors to create the powerhouse of the circulatory system. Even small errors in cardiac morphogenesis that deviate from the stereotypical process can have severe consequences for the health of the organism. Although the importance of proper cardiac morphogenesis is well established, the mechanisms responsible for controlling this process are not fully understood. Gaining insight into the cellular and molecular mechanisms underlying cardiac morphogenesis could help elucidate details about how this organ attains its shape and, importantly, what can cause this process to go awry.

The heart is the first organ to form in vertebrate embryonic development and it plays a crucial role in the distribution of oxygen and nutrients throughout the developing embryo (Buckingham et al., 2005). Vertebrate cardiac development begins with the development of a primitive linear heart tube (LHT) (Buckingham et al., 2005). The LHT consists of an interior layer of endocardial cells and an exterior layer of myocardial cells separated by an extracellular matrix, and it begins pumping blood quickly upon formation (Srivastava, 2006). The LHT then undergoes a significant transformation as it gradually forms two distinct cardiac chambers, the atrium and ventricle (Christoffels et al., 2000). Formation of these chambers involves a process referred to as cardiac looping wherein the LHT bends and twists to produce an asymmetric, S-shaped heart (Bakkers, 2011; de Pater et al., 2009; Männer, 2000; Manasek et al., 1972). Simultaneously, the walls of the heart tube expand outwards to create the characteristic shapes of

each chamber in a process known as ballooning (Moorman and Christoffels, 2003; Christoffels et al., 2000). As a result of these simultaneous processes, the ventricle and atrium are each characterized by a larger convex outer curvature (OC) and a smaller concave inner curvature (IC) (Christoffels et al., 2000). In zebrafish, this transformation from the LHT to a heart with expanded chambers and defined chamber curvatures occurs between 24 and 48 hours post fertilization (hpf) (Figure 1A-D) (Auman et al., 2007). The acquisition of these defined curvatures is essential for proper functioning of the heart, although it is not entirely clear how the cardiac tissue achieves these broad differential changes in tissue architecture.

Several models have been proposed for how the process of chamber curvature formation may be regulated (Taber, 2006). Intrinsic and extrinsic biomechanical forces like cell contractility and blood flow, respectively, are known to influence tissue morphogenesis (Heisenberg & Bellaïche, 2013; Eder et al., 2017), and the importance of these forces in aspects of cardiac morphogenesis like chamber formation and vessel development are well established (Bartman & Hove, 2005; Sidhwani & Yelon, 2019). Prior work in our lab has demonstrated that blood flow and contractility play a critical role in the formation of chamber curvatures by mediating regional changes in cell morphology (Auman et al., 2007). For example, the *weak atrium* (*wea*) mutation inhibits atrial function and decreases blood flow through the ventricle, causing zebrafish *wea* mutants to exhibit disrupted ventricular morphology with cells that fail to properly elongate correctly in the ventricular outer curvature (Auman et al., 2007). This finding adds to a body of evidence suggesting that biomechanical forces may be an important component of chamber curvature formation (Manasek et al., 1972).

In addition to biomechanical forces, it has been suggested that curvature formation could be mediated by cell behaviors like differential patterns of cell proliferation, changes in cellular

organization, or regionalized cell morphology changes (Taber, 2006; Stalsberg, 1969; Manasek et al., 1972). There is some evidence in chick demonstrating regional cell proliferation patterns during embryonic heart looping (Stalsberg, 1969; Thompson et al., 1990), although other studies in mouse and chick have found that differential patterns of cell proliferation do not likely have a significant effect on the looping process (Meilhac et al., 2004; Stalsberg, 1970). Still other experiments investigating chamber formation in chick have instead suggested that regional patterns of cell morphology changes may be one of the key factors underlying curvature formation (Manasek et al., 1972; Soufan et al., 2006). Work in mouse has provided additional evidence indicating a critical role for regional cell morphology changes in chamber curvature formation (Meilhac et al., 2004). Therefore, there is ample evidence that aligns with our group's findings that regionally confined cell shape changes may constitute one of the key mechanisms underlying curvature formation in zebrafish (Auman et al., 2007).

As with other organs, the structure of the heart is dictated by the shape and arrangement of the cells that comprise it, and while regional changes in cell morphology seem to be involved in the acquisition of distinct chamber curvatures, the specific features of cardiomyocyte shape in each region and their contributions to the overall tissue shape are not fully understood. Work from our lab has found that cardiomyocytes in the LHT tend to have relatively uniform morphologies with smaller, rounded apical surfaces, but that cells in the IC and OC appear morphologically distinct after formation of the cardiac chambers (Figure 1E-F') (Auman et al., 2007; Leerberg, unpublished). Specifically, OC cells appear to elongate primarily in the planar axis, thereby developing larger apical surface areas, while cells in the IC expand more in the apicobasal axis and develop smaller apical surface areas than OC cells (Figure 1E-F") (Auman et al., 2007; Leerberg, unpublished). These observations provide support for a model where the

squamous morphology of OC cells and cuboidal morphology of IC cells could be mediating the development of distinct inner and outer curvature tissue structures. However, it is unclear what subcellular events may be occurring to mediate these important changes in cell morphology.

The actomyosin cytoskeleton is important for maintaining the structural integrity of cells and is also a critical driver of cell size and shape in many developmental contexts (Munjal & Lecuit, 2014; Heisenberg & Bellaïche, 2013). Additionally, the inhibition of actin polymerization has been shown to inhibit heart tube looping in chick and zebrafish, indicating that actin polymerization is involved in the morphogenesis of cardiac tissues (Latacha et al., 2005; Noël et al., 2013; Manasek et al, 1972). Myosin, the central partner protein to actin, is also understood to be involved in the cardiac remodeling that underlies heart looping (Noël et al., 2013). Nevertheless, it is still not clear how exactly actomyosin activity may be facilitating this process.

The actomyosin network has multiple roles that vary depending on where it nucleates around a cell, and its localization can therefore give us important information about its potential function(s) (Clark et al., 2013; Charlène & Thomas; 2013). Research in chick has revealed that actin fibers exhibit a circumferential localization in the IC compared to cardiomyocytes in the OC which also exhibit distribution of actin filaments throughout the cytoplasmic space (Itasaki et al., 1989; Shiraishi et al., 1992). It is thought that these regional patterns of F-actin organization may be contributing to curvature formation by driving cell growth in OC cells while maintaining consistent morphologies in IC cells (Taber, 2006). Work in zebrafish has provided further support for this idea, demonstrating that F-actin remodeling can modulate cardiomyocyte morphologies and is essential for cardiac chamber formation (Deacon et al., 2010). Therefore, it seems possible that regulation of the actomyosin network could be a key factor responsible for

the unique cell morphology changes occurring in each curvature. Preliminary studies from our group provide further support for this idea, as inhibition of myosin II function and actin polymerization were found to disrupt the acquisition of curvature-specific cell morphologies (Leerberg, unpublished). Thus, while it seems clear that the actomyosin network is involved in chamber curvature formation, the field lacks a comprehensive three-dimensional analysis of the actomyosin network in cardiomyocytes of the developing chamber curvatures. Such a resource would greatly benefit our understanding of the possible roles that actomyosin plays in the acquisition of curvature-specific cell morphologies.

In considering what factors might be acting upstream of the curvature-specific regulation of cardiomyocyte morphology, we identified the transcription factor Tbx5 as an interesting candidate. Tbx5 is a member of the T-box gene family, a group of genes with numerous established roles in tissue patterning and organogenesis (Plageman & Yutzey, 2005; Greulich et al., 2011). Studies in mouse and zebrafish have found that Tbx5 is involved in regulating several aspects of cardiac morphogenesis and is important for cardiac looping (Bruneau et al., 2001; Garrity et al., 2002), a process that is essential for the formation of cardiac chambers with distinct curvature morphologies (Christoffels et al., 2004). Mice that are homozygous for a mutation in *Tbx5* fail to form cardiac chambers with distinct curvatures (Bruneau et al., 2001), and zebrafish with a loss-of-function mutation in *tbx5a*, the zebrafish paralogue of *Tbx5*, exhibit similar disruptions to chamber curvature formation (Figure 2) (Garrity et al., 2002; Tessadori et al., 2021). Importantly, Tbx5 is known to promote the expression of curvature-specific gene expression programs in mouse (Bruneau et al., 2001), suggesting that it may be involved in the acquisition of curvature-specific cell morphologies during curvature formation. Unpublished data from our lab supports this idea (Figure 2), as it was observed that *tbx5a* mutant zebrafish fail to

acquire the curvature-specific cell morphologies seen in wild-type (WT) hearts (Leerberg, unpublished). For example, measurements of apical surface area at 50 hpf show that WT cardiomyocytes in the OC expand laterally compared to cells in the IC (Figure 2C), but OC cardiomyocytes in *tbx5a* mutants fail to expand laterally and exhibit the same apical surface areas as cells in the IC (Figure 2C) (Leerberg, unpublished). Additionally, at 50 hpf WT cardiomyocytes in the IC expand along the apicobasal axis to a greater extent compared to cells in the OC, whereas in *tbx5a* mutants this differential is inverted: cells in the OC have greater apicobasal lengths than cells in the IC (Figure 2C) (Leerberg, unpublished). This evidence suggests that Tbx5a may be acting as part of a regulatory pathway that is responsible for promoting the acquisition of regionalized cell morphologies in the developing OC and IC. Understanding the specific role of Tbx5a in regulating the acquisition of these curvature-specific cell morphologies could help shine light on this critical aspect of cardiac morphogenesis.

Here, we present a novel method for quantifying the subcellular distribution of the actomyosin cytoskeleton. At 36 hpf, a developmental time point that just precedes significant changes in regionalized cell morphologies, we find that WT cardiomyocytes exhibit curvature-specific patterns of actomyosin organization. Furthermore, we see that some regionalized differences in actomyosin organization develop between 30 and 36 hpf, but that some aspects of differential actomyosin organization are likely developing even earlier. Additionally, we find that these regionalized patterns of actomyosin organization are mitigated in *tbx5a* mutants. Given that curvature-specific differences in cell morphology begin to occur soon after we observe these curvature-specific differences in actomyosin organization, we speculate that differential patterning of actomyosin in the developing curvatures may be related to the development of regionalized cell morphologies. These findings reveal important details about the mechanisms

underlying a key aspect of cardiac morphogenesis and improve our understanding of how disruptions to these mechanisms may contribute to congenital heart disease.

Figure 1. Chamber curvature formation and regionalized cell morphology changes in the developing zebrafish heart. (A) Diagram showing the LHT at 24 hpf. Arrow and arrowhead denote regions that will become the OC of the ventricle and atrium, respectively. (B) Expanded cardiac chambers at 48 hpf showing the OC and IC of the ventricle. (C, D) Live image showing a dorsal view of the LHT in a *Tg(myl7:egfp)* zebrafish at 24 hpf (C) and a frontal view of a 48 hpf heart with expanded chambers (D). (E, E') Partial 3D reconstructions of wild-type (WT) ventricular OC (E) or IC (E') at 50 hpf. Immunostaining labels Cdh2 in lateral cell membranes. Our working definitions of OC and IC are informed by the regions of highest and lowest expression of *nppa*, respectively (Auman et al., 2007). Briefly, both regions begin just proximal to the atrioventricular canal (AVC); the OC ends 2/3 of the way from the AVC to the outflow tract (OFT), and the IC ends halfway between the AVC and OFT (Figure 2A). Scale bar: 20 μm. (F-F") Sagittal sections through the WT (D) ventricle at 50 hpf. Boxed regions in (F) are highlighted in (F', F"). Brackets show apicobasal length and arrows highlight lateral widths at the apical and basal extremes of individual cells. OC cells (F') exhibit notable basal constriction, whereas IC cells (F") exhibit notable apical constriction. The material in panels (A-D) is adapted from Auman et al., 2007. Panels (E-F") are adapted from unpublished work performed by Dena M. Leerberg.

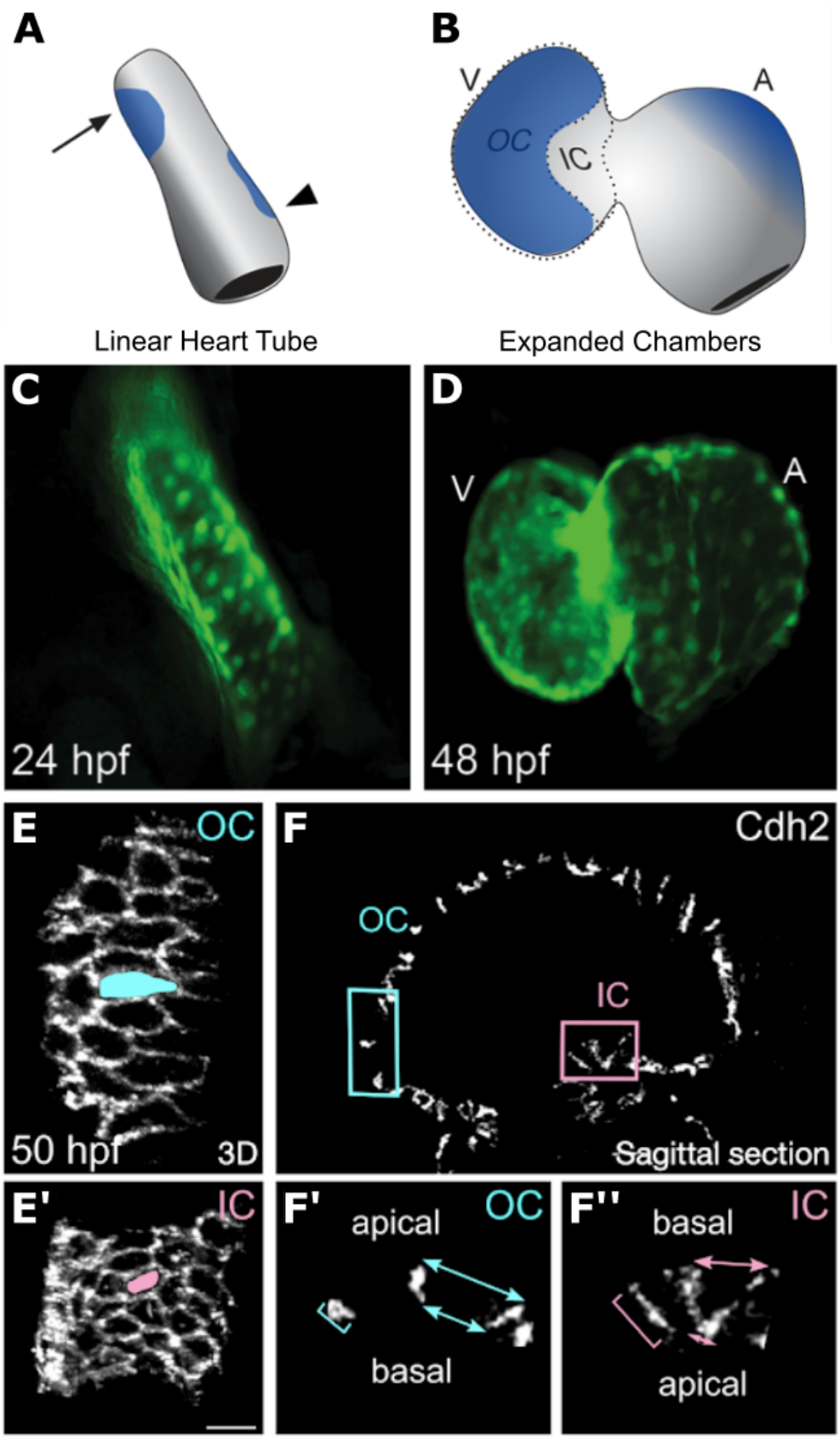
A
B
V
A
OC
IC
Linear Heart Tube
Expanded Chambers
C
D
V
A
24 hpf
48 hpf
E
OC
F
Cdh2
OC
IC
50 hpf
3D
Sagittal section
E'
IC
F'
apical
OC
basal
F''
basal
IC
apical

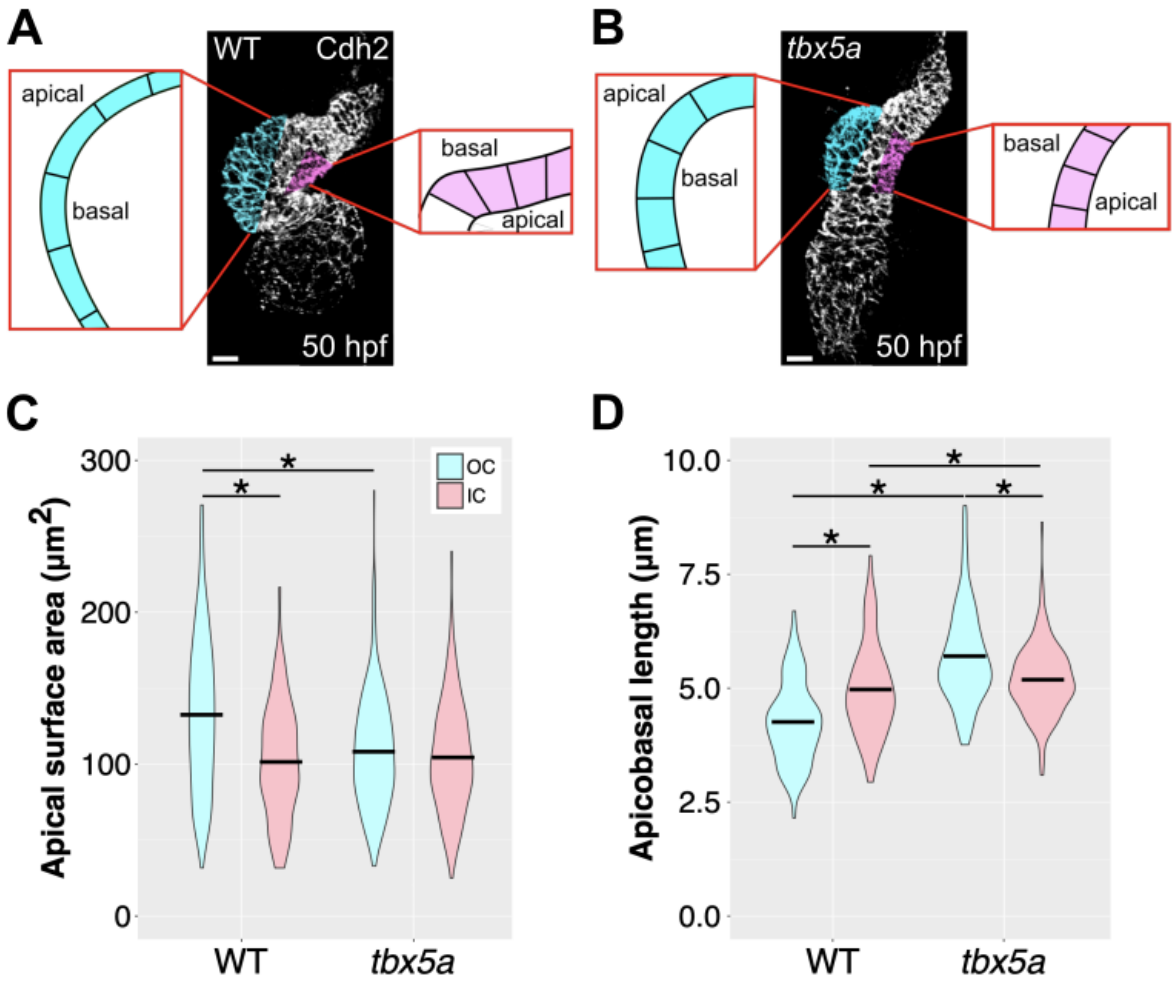

Figure 2. Tbx5a promotes the acquisition of curvature-specific cell morphologies. (A, B) 3D reconstructions of WT (A) and *tbx5a* mutant (B) hearts at 50 hpf stained for N-cadherin (Cdh2) to mark cell membranes. Aqua and pink areas mark the ventricular OC and IC, respectively, based on our working definitions of these regions (Figure 1). Schematics depict sagittal views of the myocardial wall. In WT, OC cells are extended along the planar axis, relatively flat, and basally constricted compared to IC cells, which are cuboidal and apically constricted. In contrast, *tbx5a* mutant OC cells fail to extend along the planar axis and instead extend along the apicobasal axis, and *tbx5a* mutant IC cells do not exhibit apical constriction. Scale bars: 20 µm. (C) Violin plot shows mean and distribution of apical surface area for OC (aqua) and IC (pink) cells from WT and *tbx5a* hearts at 50 hpf. (D) Violin plot shows mean and distribution of apicobasal length. n≥4 hearts; 85<n>221 cells per genotype, stage, and region. Asterisks: $p<0.05$, Wilcoxon test. The material in this figure is adapted from unpublished work performed by Dena M. Leerberg.

RESULTS

Subcellular distribution of the actomyosin network differs between OC and IC cardiomyocytes

Given the observed morphological differences between OC and IC cardiomyocytes (Figure 1, Figure 2), we were curious about what types of subcellular changes might be mediating the development of these curvature-specific cell morphologies. Since prior studies and our own preliminary data demonstrate the importance of the actomyosin network in chamber curvature development (Manasek et al., 1972; Latacha et al., 2005; Voronov et al., 2004; Noël et al., 2013) as well as the acquisition of curvature-specific cell shapes (Leerberg, unpublished), we chose to focus our attention on the subcellular organization of F-actin and p-Myo. Specifically, we hypothesized that the differential cell morphologies in the OC and IC are accompanied by curvature-specific patterns of subcellular F-actin and p-Myo organization.

To investigate the distribution of the actomyosin network within cardiomyocytes, we first developed a technique to analyze the apicobasal distribution of F-actin and p-Myo in individual cells. As shown in Figure 3A-A", we utilized the oblique slicer feature of Imaris to capture snapshots of individual cells (see Materials and Methods for more detail). Using Fiji, we measured the distribution of fluorescence signal intensity values for F-actin and p-Myo along the center of each cell from its basal membrane to its apical membrane (Figure 3A"). In choosing what developmental stages to analyze, we considered preliminary studies showing that inhibition of actin polymerization or myosin activity from 24-36 hpf (but not from 36-48 hpf) limits the apical growth of OC cardiomyocytes (Leerberg, unpublished). We therefore reasoned that examining actomyosin dynamics between 24 and 36 hpf would help us understand the regulation

and function(s) of this network during this time frame, and we began this analysis by evaluating cardiomyocytes at 36 hpf.

In 36 hpf WT hearts, we observed two primary differences in the apicobasal distribution of actomyosin between OC and IC cardiomyocytes (Figure 3B-G). In OC cardiomyocytes, both F-actin and p-Myo are primarily localized to basal cell membranes as opposed to apical membranes (Figure 3B, B', F, G). Comparatively, apical deposition is more evident in IC cells than OC cells, resulting in a more balanced apical versus basal distribution (Figure 3C, C', F, G). The trends observed for F-actin are generally similar to the trends observed for p-Myo, except that in IC cells the proportion of basal to apical F-actin (Figure 3C, E) is slightly greater than the proportion of basal to apical p-Myo (Figure 3C', E') which appears to have more comparable localization between these membranes (Figure 3F, G).

These findings demonstrate that the patterns of actomyosin organization in OC cells are indeed distinct from the patterns in IC cells (Figure 3B-G). F-actin and p-Myo are predominantly distributed in basal membranes as opposed to apical membranes in OC cells, while IC cells exhibit a more comparable apicobasal distribution of actomyosin compared to OC to cells. These results lend support to the idea that curvature-specific patterns of actomyosin organization could be related to the subsequent divergence in morphologies between OC and IC cells

Actomyosin organization is disrupted in *tbx5a* mutants

Work from our lab (Figure 2) has demonstrated that *tbx5a* mutants fail to develop the differential OC and IC cardiomyocyte morphologies seen in the curvatures of WT hearts. Since *tbx5a* seems to be necessary for the development of curvature-specific cell morphologies, we

wanted to test whether *tbx5a* promotes the acquisition of curvature-specific patterns of actomyosin organization, and in this way may promote particular cell morphologies.

At 36 hpf, *tbx5a* mutant cardiomyocytes in the OC exhibit a greater proportion of both F-actin and p-Myo in apical membranes compared to WT cells in the OC (Figure 3B, B', F, G). In the IC, the relative proportions of F-actin and p-Myo distributed in the basal membranes of *tbx5a* mutant cardiomyocytes (Figure 3E, E', F, G) are greater than the proportions of basal F-actin and p-Myo in WT IC cells (Figure 3C, C', F, G). In summary, our findings demonstrate that the differential patterns of actomyosin organization observed in OC and IC cardiomyocytes are perturbed in *tbx5a* mutants. This result suggests that a Tbx5a-regulated pathway mediates the development of curvature-specific actomyosin organization patterns prior to 36 hpf, a stage where the morphologies of inner and outer curvature cardiomyocytes begin to diversify.

Figure 3. Apicobasal distribution of the actomyosin network differs between OC and IC cardiomyocytes, and actomyosin organization is disrupted in *tbx5a* mutants. (A-A") Scheme for collecting individual cell images for apicobasal distribution of F-actin and p-Myosin. (A) WT ventricle at 36 hpf stained for F-actin (green), p-Myo (red), and activated leukocyte cell adhesion molecule a (Alcama, blue). Alcama (blue) marks lateral cell membranes. OC and IC labels mark the outer and inner curvatures. (A') Same ventricle as in (A), showing only the Alcama channel. Double white line indicates the position of an oblique slicer. For each cardiomyocyte in the OC and IC, a 1.42 µm slicer was placed to bisect the center of the cell. The "volume" of the ventricle was removed, leaving a 1.42 µm thick partial reconstruction at the position of the slicer, as seen in (A"). See Materials and Methods for more detail. (A") Cell encircled by the dashed white line in (A') showing F-actin, p-Myo, and Alcama fluorescent channels. Apical and basal membranes are labeled and indicated by arrowheads and arrows, respectively. Solid yellow line demonstrates the area where apicobasal distribution measurements were collected in the middle of cells. (B-E') Representative images of OC (B-B', D-D') and IC (C-C', E-E') cardiomyocytes at 36 hpf from WT (B-C') and *tbx5a* mutant (D-E') animals showing staining for F-actin and p-Myo. (F, G) Graphs showing the basal (left) to apical (right) distribution of relative fluorescence intensity for F-actin (F) and p-Myo (G) for cells in the OC and IC. WT samples are shown in black, *tbx5a* mutant samples are shown in red. Gray shading around each line represents the standard error of the mean (SEM). n = 5 hearts, n>33 cells per genotype. Scale bars: 20 µm (A, A'); 2 µm (A", B-E').

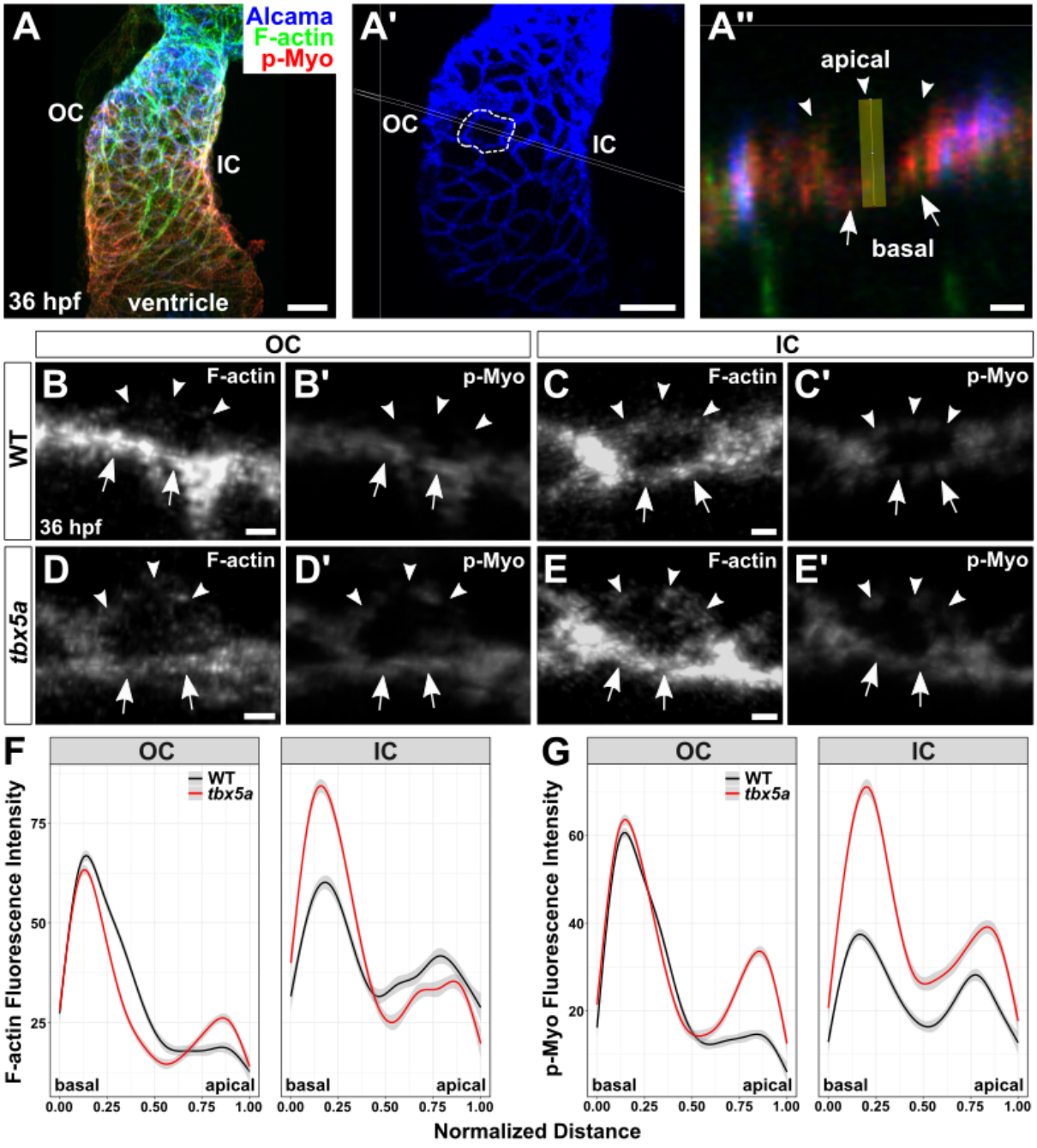
A
Alcama
F-actin
p-Myo
OC
IC
36 hpf
ventricle
A'
OC
IC
A''
apical
basal
OC
IC
WT
B
F-actin
B'
p-Myo
C
F-actin
C'
p-Myo
36 hpf
tbx5a
D
F-actin
D'
p-Myo
E
F-actin
E'
p-Myo
F
OC
IC
WT
tbx5a
F-actin Fluorescence Intensity
75
50
25
basal
apical
0.00
0.25
0.50
0.75
1.00
G
OC
IC
WT
tbx5a
p-Myo Fluorescence Intensity
60
40
20
basal
apical
Normalized Distance

Improving our understanding of subcellular actomyosin organization

Although our initial analysis provided an intriguing and novel look into the subcellular organization of actomyosin, we recognized that this analysis missed some key elements of actomyosin distribution. Specifically, our initial analysis did not capture actomyosin localized in the lateral membranes. This pool of actomyosin is particularly important in maintaining cell-cell adhesions through partnerships with adherens and other junctions. We therefore set out to develop a technique that allowed us to gather information about actomyosin distribution in these lateral membranes, as well as in the apical and basal membranes. Additionally, to begin to understand how the observed patterns of actomyosin emerge over time, we decided to include 30 hpf wild-type embryos in this analysis.

Because our goal was to develop a system that would provide a more comprehensive picture of how the actomyosin cytoskeleton is organized, we recognized that rigorously utilizing consistent imaging settings would allow us to better compare relative fluorescence intensities within and between experimental groups. This is an important distinction from the prior method of analysis used in Figure 3 where raw fluorescence intensity data could not be compared between samples, as we adjusted the laser intensities for samples with excessively strong or weak signals due to variance in staining intensity. We also made minor changes to our antibody staining protocol to facilitate the best possible resolution of the fluorescent markers. One notable change is that instead of staining for Alcama to mark lateral cell membranes, we opted to use *Tg(myl7:EGFP-Hsa.HRAS)*^{s883} transgenic fish to allow for visualization of eGFP uniformly along cardiomyocyte membranes (Figure 4A).

Another drawback of the image analysis technique described in Figure 3 is that this method only captured snapshots of cells through one plane: an arbitrary X axis. While the

information about actomyosin distribution obtained from this method is useful, it is possible that wherever the oblique slicer is positioned in the cell may not necessarily represent the distribution patterns for all other regions of the cell. For this reason, we chose to collect snapshots of cell slices from two planes. The two slicers were perpendicularly positioned such that they each bisected a single cell (Figure 4A'), thus allowing us to capture snapshots of the cell in its X and Y axes (Figure 4A", A'"), where X and Y are perpendicular, lateral axes, and Z is the apicobasal axis (Figure 4A'). By capturing snapshots of each cell in two planes (Figure 4A'-A'") instead of one (Figure 3A, A'), we were able to double the data obtained from each cell and therefore increase the likelihood of accurately measuring what the actomyosin network looks like in a given cell.

Differential patterns of actomyosin organization are present between basal, apical, and lateral membranes of OC and IC cardiomyocytes at 36 hpf

Given the observed differences in apicobasal distribution of actomyosin between WT OC and IC cardiomyocytes at 36 hpf (Figure 3), we were curious to see if this alternative analysis technique better informs our understanding of how subcellular actomyosin organization differs between curvatures. In WT hearts at 36 hpf, we observed that cells in the IC have more F-actin and p-Myo in their apical membranes than OC cells do (Figure 4D-E', H-H'). F-actin levels in lateral membranes are also greater in IC cells than in OC cells (Figure 4D-E', H-H'). In contrast to these differences, we observe that OC and IC cells also exhibit some similarities in actomyosin organization: they have comparable amounts of F-actin in their basal membranes (Figure 4H), comparable amounts of p-Myo in their basal membranes (Figure 4H), and comparable amounts of p-Myo in their lateral membranes (Figure 4H').

An added benefit of this analysis is that it also provides an illuminating snapshot of the relative distribution of actomyosin between the apical, basal, and lateral cell membranes that expands on the type of data collected in Figure 3. The relative proportions of F-actin (Figure 4I) and p-Myo (Figure 4I') signal intensity in each membrane highlight that at 36 hpf the majority of F-actin and p-Myo in WT cells from both curvatures is localized in lateral membranes (Figure 4D-E', I-I'). This is an important observation that expands our understanding of subcellular actomyosin organization and was not captured in our prior analysis. Additionally, the proportions of F-actin and p-Myo are greater in basal membranes than apical membranes for WT cells of both curvatures (Figure 4D-E', I, I'). Comparing between the curvatures, we see that the proportion of basal F-actin at 36 hpf is greater in WT OC cells than IC cells (Figure 4D, E, I). This observation mirrors our findings from the analysis in Figure 3 and highlights a difference in organization between the OC and IC that was not seen by evaluating the raw fluorescence data intensity data. Also, we find that the proportion of lateral F-actin is higher in WT IC cells than OC cells (Figure 4D, E, I). The proportions of p-Myo distribution were not significantly different between OC and IC cells at 36 hpf, nor were the proportions of apical F-actin (Figure 4I-I'). It should be noted that rescaling pixel signal intensity data into percentages may be collapsing some of the variance between measurements, potentially masking some significant differences that can be seen in the raw fluorescence intensity data. Taken together, these data reinforce our prior observations showing that WT OC cells exhibit greater basal localization of actomyosin while IC cells exhibit more equivalent localization of actomyosin between basal and apical membranes. An important addition to our prior observations is the finding that WT IC cells exhibit greater deposition of F-actin in lateral membranes compared to OC cells.

Compared to the analysis presented in Figure 3, the actomyosin analysis technique described in Figure 4A-A''' provided us with a more holistic view of actomyosin organization throughout a given cell by revealing previously unobserved actomyosin in the lateral membranes and allowing us to directly compare levels of F-actin and p-Myo between membranes and curvatures at 36 hpf. Validating our findings in Figure 3, we observed that WT cardiomyocytes in the IC at 36 hpf exhibit increased apical localization of actomyosin compared to cells in the OC (Figure 4D-E', H-H'). Expanding on our findings in Figure 3, we observed that curvature-specific differences in F-actin are also present in lateral cell membranes with OC cells exhibiting decreased lateral localization of F-actin compared to IC cells (Figure 4D, E, H, I). Also, we found that p-Myo in lateral cell membranes is comparable between OC and IC cells (Figure 4H'), prompting us to consider how the apical pool of p-Myo may be more relevant to the acquisition of curvature-specific cell morphologies than p-Myo in basal or lateral membranes. We were somewhat surprised to see that localization of p-Myo appears relatively similar between OC and IC cells in basal membranes (Figure 4H', I') because we did not observe this trend in our p-Myo apicobasal distribution data (Figure 3B', C', G). Nevertheless, these data demonstrate that significant differences in actomyosin organization exist between OC and IC cardiomyocytes at 36 hpf and bolster our hypothesis that differential patterns of actomyosin organization between OC and IC cells are connected to the eventual curvature-specific cell morphologies

Overall levels of F-actin and p-Myo are reduced and curvature-specific patterns of actomyosin organization are disrupted in *tbx5a* mutant cardiomyocytes at 36 hpf

Considering the disrupted patterns of apicobasal actomyosin distribution we observed in Figure 3, we were curious to observe how the actual levels of actomyosin in *tbx5a* mutant cells

compared to the levels seen in WT cells. We wondered if the failure to acquire curvature-specific cell morphologies seen in *tbx5a* mutants could be related to *tbx5a* cardiomyocytes possessing inappropriate amounts of F-actin and p-Myo. Indeed, relative to WT cells from both curvatures at 36 hpf, levels of F-actin in all membranes are reduced substantially in *tbx5a* cells at 36 hpf (Figure 4D, E, F, G, H) and levels of p-Myo in *tbx5a* cells are also moderately reduced compared to WT cells (Figure 4D', E', F', G', H'). These findings demonstrate one potential mechanism for why the morphologies of *tbx5a* cardiomyocytes are so disrupted compared to WT cardiomyocytes.

Our subcellular organization analyses highlight several intriguing trends about the organization of actomyosin in WT cardiomyocytes at 36 hpf and how organization differs between curvatures. In WT cardiomyocytes at 36 hpf, we observed that IC cells have greater levels of apical and lateral F-actin compared to OC cells (Figure 4D, E, H), as well as greater levels of apical p-Myo than OC cells (Figure 4D', E', H'). In addition, OC cells have comparably greater basal localization of F-actin compared to IC cells (Figure 4D, D', I). Remarkably, many of these curvature-specific differences in actomyosin organization are absent in *tbx5a* mutants. In contrast to the differential actomyosin levels in apical membranes of WT cells, apical F-actin and p-Myo levels are similar between OC and IC *tbx5a* cells (Figure 4F-G', H, H'). The proportion of basal F-actin is also comparable between OC and IC *tbx5a* cells (Figure 4F, G, I), eliminating the WT pattern of increased basal F-actin in OC cells relative to IC cells (Figure 4F, D, I). Deviating also from the WT pattern of increased F-actin localization in lateral membranes of IC cells compared to OC cells (Figure 4D, E, I), the proportion of lateral F-actin is similar between OC and IC *tbx5a* cells (Figure 4F, G, I). It is worth noting here that although the actual levels of lateral F-actin are greater in *tbx5a* IC cells compared to OC cells (Figure 4H), mirroring the trend

seen in WT (Figure 4H), the relative proportions of F-actin in lateral membranes remain similar between OC and IC cells in *tbx5a* mutants (Figure 4I). This observation highlights the value of evaluating the proportionality data presented in Figure 4I and I' in addition to raw data. All together, these data validate prior observations from Figure 3 that patterns of apical and basal actomyosin localization are disrupted in *tbx5a* mutants. The data also add new information that reveals additional disruptions to the curvature-specific patterns of actomyosin localization in lateral cell membranes. Importantly, the data also demonstrate that one of the most significant differences between WT and *tbx5a* mutant cells is the overall reduction in the actual amounts of actomyosin present in cell membranes, highlighting a previously unappreciated phenotype of the actomyosin network in *tbx5a* mutants.

Curvature-specific actomyosin organization patterns are present by 30 hpf and develop further by 36 hpf

Preliminary data from our group show that the morphologies of OC and IC cells begin to diverge considerably between 36 and 50 hpf (Figure 2; Leerberg, unpublished). Together with our observations presented in Figures 3 and 4 that curvature-specific patterns of actomyosin organization are present by 36 hpf, we hypothesize that curvature-specific remodeling of the actomyosin cytoskeleton prior to 36 hpf may be promoting the subsequent acquisition of curvature-specific cell morphologies from 36 hpf onwards. However, our experiments thus far do not highlight how these patterns of actomyosin organization emerge over time, and we therefore decided to include 30 hpf wild-type embryos in this analysis.

Upon analysis of WT 30 hpf cardiomyocytes, we find that some curvature-specific trends observed in 36 hpf wild-type cells are already apparent at the earlier developmental stage. For

example, at 30 hpf, we observe that cells in the OC (Figure 4B) already exhibit greater basal localization of F-actin compared to IC cells (Figure 4C, H, I). We also observe at 30 hpf that WT cells in the IC (Figure 4C') exhibit greater apical localization of p-Myo compared to WT cells in the OC (Figure 4B', H', I'). These data suggest that some aspects of differential actomyosin organization between OC and IC cells develop prior to 30 hpf.

Although it is not appropriate to directly compare the raw values of fluorescence intensity between 30 and 36 hpf samples due to inherent variance in antibody staining between experiments, we can make comparisons between the relative proportions of actomyosin localized in cell membranes at each time point. While some curvature-specific differences in actomyosin organization are present by 30 hpf, we also observed some changes in actomyosin organization between 30 and 36 hpf in WT cells. At 30 hpf we see the proportion of F-actin in lateral membranes is comparable between OC and IC WT cells (Figure 4B, C, H, I), but by 36 hpf cells in the IC exhibit a greater proportion of lateral F-actin than cells in the OC (Figure 4D, E, H, I). Additionally, the proportion of apical F-actin is comparable between OC and IC WT cells at 30 hpf (Figure 4B, C, H, I), but by 36 hpf we observe that cells in the IC exhibit increased apical localization of F-actin relative to cells in the OC (Figure 4D, E, H). Interestingly, while there does appear to be changes to the organization of F-actin in WT cells from 30 to 36 hpf, there does not appear to be any significant changes in the organization of p-Myo between these times (Figure 4B', C', D', E', I, I'). We observe that lateral and basal localization of p-Myo is comparable between OC and IC WT cells at 30 hpf and this trend remains present at 36 hpf (Figure 4B', C', D', E', I, I'). Additionally, apical localization of p-Myo is greater in IC WT cells compared to OC cells at 30 hpf and this trend remains consistent by 36 hpf (Figure 4B', C', D', E', I, I').

An unexpected benefit of including 30 hpf WT cells in this analysis comes from comparing 30 hpf WT data to that of 36 hpf *tbx5a* mutants and finding some striking similarities. For example, we find that the proportions of lateral and apical F-actin between OC and IC cells are comparable in WT cells at 30 hpf (Figure 4B, C, H'), and we observe the same trend for *tbx5a* mutant hearts at 36 hpf (Figure 4F, G, I). Moreover, we see that the proportions of basal and lateral p-Myo in WT cells at 30 hpf are comparable between curvatures (Figure 4B', C', I'), mirroring the comparable proportions of basal and lateral p-Myo between OC and IC cells in *tbx5a* mutants at 36 hpf. Perhaps these similarities suggest that the *tbx5a* actomyosin cytoskeleton is locked in a developmentally immature state.

Altogether these data suggest that while some curvature-specific differences in F-actin organization already exist at 30 hpf, others emerge between 30 and 36 hpf. In addition, the data show that the actomyosin organization patterns in *tbx5a* mutants in some ways resemble an earlier stage of WT development, suggesting that Tbx5a may be regulating the emergence of curvature-specific patterns of actomyosin organization that precede differential changes in cell morphology.

Figure 4. Actomyosin organization patterns shift over time and differ between OC and IC cardiomyocytes. (A-A‴) Scheme for collecting individual cell images to evaluate the subcellular distribution of F-actin and p-Myo. (A) Ventricle of a *Tg(myl7:EGFP-Hsa.HRAS)*^{s883} animal at 30 hpf stained for F-actin (red) and p-Myo (blue). Cell membranes are labeled green with GFP by the *Tg(myl7:EGFP-Hsa.HRAS)*^{s883} transgene. (A') Same ventricle as in (A), showing only the GFP channel with two 1.42 µm slicers bisecting the cells shown in (A", A‴). Double white line indicates the position of an oblique slicer. For each cardiomyocyte in the OC and IC, one slicer was placed to bisect the cell in one lateral axis (slicer X), and another slicer was placed to bisect the cell in an approximately perpendicular lateral axis (slicer Y). The "volume" of the ventricle was removed, leaving a 1.42 µm thick partial reconstruction at the position of each "X" and "Y" slicer, as seen in (A") and (A‴). (A", A‴) Cell encircled by the dashed white line in (A') as seen through the sections produced by slicer X (A") and slicer Y (A‴). Demonstration of Fiji image analysis technique used to measure mean fluorescence intensity of F-actin and p-Myo along the basal, apical, and lateral cell membranes. The yellow lines demonstrate how measurements would be taken for apical and basal membranes (A") and lateral membranes (A‴). See Materials and Methods for more detail. (D-E') Representative images of 30 hpf WT OC (B, B') and IC (C, C') cardiomyocytes stained for F-actin and p-Myo. (D-G') Representative images of 36 hpf WT (D-E') and *tbx5a* (F-G') cardiomyocytes in the OC and IC stained for F-actin and p-Myo. (H, H') Stacked bar chart showing the raw fluorescence signal intensity values (rfu) for F-actin (H) and p-Myo (H') in cardiomyocytes from each age, genotype, and curvature. Basal membrane values are shown in yellow, lateral membrane values in turquoise, and apical membrane values in purple. Lines with asterisks indicate significant differences between values ($p<0.05$, Wilcoxon test). All differences between 36 hpf WT and *tbx5a* raw values are significant; all percentage differences are significant except for apical F-actin and p-Myo in the IC and basal p-Myo in both curvatures. N = 5 hearts for each genotype and age. 30 hpf WT: n = 210 (OC: n = 131, IC: n = 78). 36 hpf WT: n = 181 (OC: n = 112, IC: n = 69). 36 hpf *tbx5a*: n = 212 (OC: n = 131, IC: n = 81). Scale bars: 20 µm (A), 2 µm (all others).

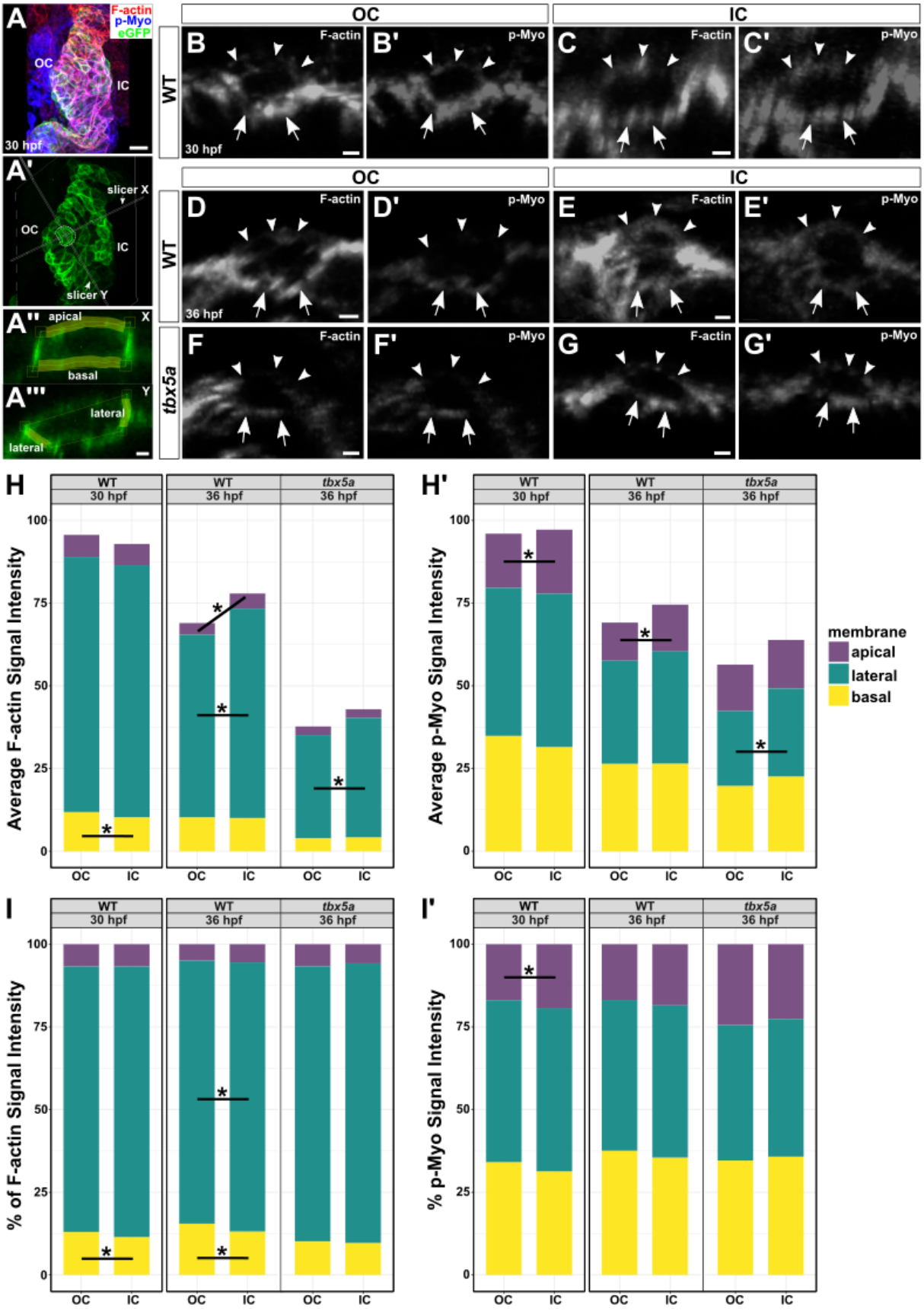
A
F-actin
p-Myo
eGFP
OC
IC
30 hpf
A'
slicer X
slicer Y
A''
apical
basal
X
A'''
lateral
Y
OC
IC
WT
tbx5a
B
B'
C
C'
D
D'
E
E'
F
F'
G
G'
F-actin
p-Myo
30 hpf
36 hpf
H
H'
I
I'
WT
30 hpf
WT
36 hpf
tbx5a
36 hpf
Average F-actin Signal Intensity
Average p-Myo Signal Intensity
% of F-actin Signal Intensity
% p-Myo Signal Intensity
membrane
apical
lateral
basal
0
25
50
75
100
*

Patterns of actomyosin organization differ between cardiomyocytes in proximal and distal regions of the ventricle

The data we have presented thus far demonstrate multiple examples of differential patterns of actomyosin organization between OC and IC cells in WT hearts. However, we recognize that the territories we define as the outer and inner curvatures are defined based on curvature-specific gene expression patterns that do not necessarily relate to aspects of curvature-specific development like changes in cell morphology. We therefore considered that smaller subpopulations of cells within our working definitions of the curvatures may be particularly integral in driving tissue morphogenesis, and that combining actomyosin organization data for all cardiomyocytes in a curvature could mask interesting and biologically relevant trends. To probe whether we could identify subpopulations with interesting patterns of actomyosin organization, we recorded whether each analyzed cell reported in Figure 4 resided in the proximal or distal half of each curvature, where the proximal region of each curvature abuts the atrioventricular canal (AVC) and the distal region of each curvature is nearer to the outflow tract (OFT) (Figure 5A).

When comparing the actomyosin localization of cells in different curvature subregions, we observed a number of interesting trends. For example, in WT hearts at 36 hpf, distal cardiomyocytes in both curvatures (Figure 5G, I) have greater average levels of apical F-actin than proximal cardiomyocytes (Figure 5F, H, N) and that average basal F-actin levels are greater in proximal OC cardiomyocytes (Figure 5F) compared to distal OC cardiomyocytes (Figure 5G, O). In contrast, levels of basal F-actin are similar between proximal and distal WT cardiomyocytes in the IC (Figure 5H, I, O). We found these findings intriguing, as they indicate that regulation of curvature-specific actomyosin patterning could be occurring on an even more granular level than what is represented by looking at data for an entire curvature.

Another interesting finding from dividing F-actin organization data into proximal and distal components relates to the development of curvature-specific F-actin organization patterns over time. We noted that apical F-actin levels in 36 hpf WT cells are higher in distal cardiomyocytes compared to proximal cardiomyocytes from both curvatures, but at 30 hpf levels of apical F-actin are similar between proximal and distal cells (Figure 5D, E, N). Also, we observed that basal F-actin levels in the OC are higher in proximal cells (Figure 5F, H) compared to distal cells (Figure 5F, G) at both 30 and 36 hpf, whereas levels of basal F-actin were comparable between proximal and distal cells of the IC at both time points (Figure 5D, E, H, I, O).

While analyzing these data we realized that comparing the basal to apical ratios of F-actin could help further highlight some of curvature-specific and subregionalized differentials. For example, in WT cells at 36 hpf, there is a striking and significantly higher ratio of basal to apical F-actin in proximal cardiomyocytes of the OC (Figure 5F) compared to distal cardiomyocytes of the OC (Figure 5G, P). Although the ratio of basal to apical F-actin is also higher in proximal WT cells in the IC at 36 hpf (Figure 5H, P) compared to distal cells at this time (Figure 5I, P), this differential is smaller than the differential between proximal and distal OC cells (Figure 5F, G, P). This finding aligns with our key earlier observations that IC cells exhibit comparatively more apical F-actin than OC cells (Figure 3, Figure 4), and highlights that the proportion of F-actin in various membrane pools is an important factor to consider alongside the raw values. Overall, these observations reveal that there are in fact regionally defined subpopulations that exhibit distinct F-actin organization beyond the curvature-specific differences highlighted in Figures 3 and 4

Patterns of actomyosin organization in proximal and distal cardiomyocytes are disrupted in *tbx5a* mutants

Data from 36 hpf WT hearts suggest that proximal and distal regions of each curvature exhibit differential subcellular F-actin organization. Given our observations in Figures 3 and 4 that *tbx5a* mutants fail to acquire some of the curvature-specific patterns of actomyosin organization seen in WT hearts at 36 hpf, we wondered whether *tbx5a* mutants may also fail to develop differential patterns of actomyosin between the proximal and distal regions of the curvatures.

We observed that, similar to WT, *tbx5a* mutants exhibit greater levels of apical F-actin in distal cells (Figure 5K, M) compared to proximal cells of both curvatures (Figure 5J, L, N). In contrast, while we observed that basal F-actin levels in WT hearts are greater in cells in the proximal OC compared to cells in the distal OC (Figure 5O), we find that the levels of basal F-actin in *tbx5a* mutants are similar between proximal and distal regions of the OC (Figure 5J, K, O). This result is interesting to consider alongside our observations of basal F-actin in Figure 4, as these findings demonstrate that *tbx5a* mutants fail to develop both curvature-specific patterns of basal F-actin organization as well as subregional patterns of basal F-actin organization within the curvatures. Moreover, it is intriguing to consider how *tbx5a* mutants are able to develop distinct patterns of apical F-actin organization between the proximal and distal subregions of each curvature but fail to develop subregional differences in basal F-actin organization in both curvatures.

Taken together, these data reinforce observations from Figures 3 and 4 that *tbx5a* mutants fail to develop multiple patterns of subcellular F-actin organization that are seen in WT cells. From these data, we also find that the disruptions to F-actin organization seen in *tbx5a* mutants

include a failure to develop some differential patterns of subcellular F-actin organization between curvatures as well as between subregions of the curvatures. Importantly, these results also speak to the importance of evaluating patterns of actomyosin organization on a more granular level than simply considering distinctions between entire curvatures.

Figure 5. Subcellular F-actin localization patterns differ between regions of each curvature, and their organization is disrupted in *tbx5a* mutants. (A) Image of a 50 hpf WT ventricle stained for Cdh2 with blue shading in the OC and pink shading in the IC. Diagrams to the left and right of the image represent the proximal and distal regions within each curvature. (B-E) Representative images of 30 hpf WT CMs stained for F-actin in the proximal (B) and distal (C) regions of the OC; CMs in the proximal (D) and distal (E) regions of the IC. Arrowheads denote apical membranes and arrows denote basal membranes. Representative images of 36 hpf WT (F-I) and *tbx5a* (J-M) CMs stained for F-actin in the proximal and distal regions of each curvature. (N-P) Violin plots showing the average apical (N), basal (O) and basal/apical ratio (P) of F-actin fluorescence intensity for WT and *tbx5a* CMs from proximal and distal regions of each curvature. Lines with asterisks indicate significant differences between values ($p<0.05$, Wilcoxon). n = 5 hearts for each genotype and time point, n>181 cells per curvature. n = 5 hearts for each genotype and age. 30 hpf WT: n = 210 (OC: n = 131, IC: n = 78). 36 hpf WT: n = 181 (OC: n = 112, IC: n = 69). 36 hpf *tbx5a*: n = 212 (OC: n = 131, IC: n = 81). Scale bars: 2 μm.

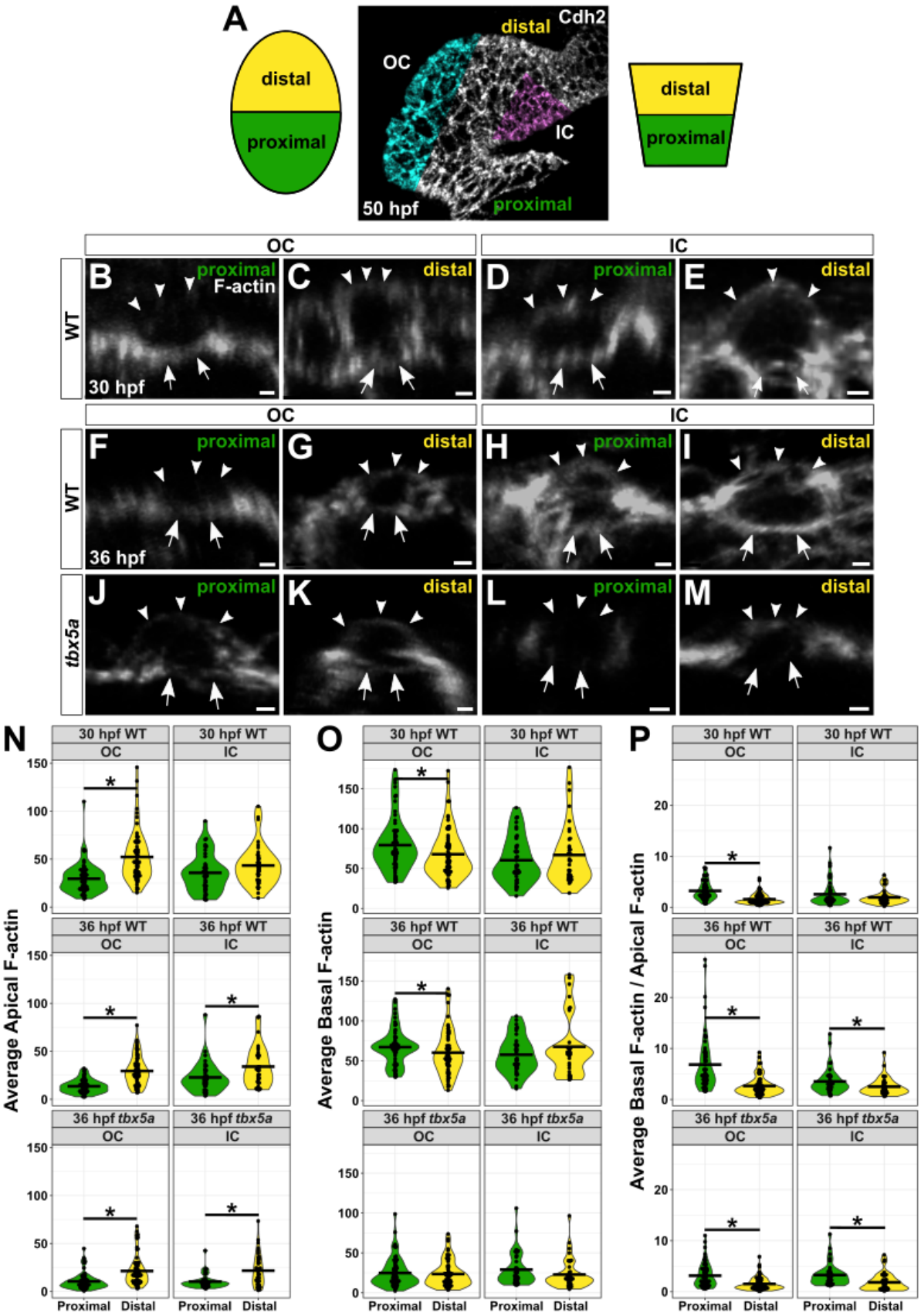
A
distal
proximal
Cdh2
distal
OC
IC
50 hpf
proximal
distal
proximal
OC
IC
WT
B proximal F-actin
C distal
D proximal
E distal
30 hpf
OC
IC
WT
F proximal
G distal
H proximal
I distal
36 hpf
tbx5a
J proximal
K distal
L proximal
M distal
N
Average Apical F-actin
30 hpf WT
36 hpf WT
36 hpf tbx5a
OC
IC
Proximal
Distal
O
Average Basal F-actin
P
Average Basal F-actin / Apical F-actin

DISCUSSION

The development of distinctly shaped inner and outer chamber curvatures is critical for the physiological functions of the heart, although the subcellular mechanisms underlying the development of these unique curvature morphologies are not fully understood. Here, we strove to develop a comprehensive approach to identify distinctions between the actomyosin organization in inner and outer curvature cardiomyocytes that might drive regional changes in cell morphologies. We examined subcellular actomyosin organization in WT cardiomyocytes at 36 hpf, a stage that precedes significant changes in cell morphology (Leerberg, unpublished), and observed differential localization of actomyosin between OC and IC cells in apical, basal, and lateral cell membranes. We also surveyed actomyosin organization in *tbx5a* mutant hearts at 36 hpf and observed that many of the curvature-specific patterns of actomyosin organization seen between OC and IC WT cells are absent or markedly reduced in *tbx5a* mutants. We investigated WT hearts at 30 hpf and found that some of the curvature-specific differences in actomyosin organization seen in 36 hpf hearts are present by this time, indicating that curvature-specific organization develops even earlier than 30 hpf. Expanding our analysis of actomyosin organization to subregions of the curvatures, we observe some differential F-actin organization between cells located in the proximal and distal regions of both curvatures, revealing previously unappreciated patterns of actomyosin organization between subregions of the OC and IC.

Prior studies demonstrate that actomyosin activity is required for chamber curvature formation (Noël et al, 2013; Manasek et al., 1972), although the precise subcellular organization of the actomyosin network and its exact roles in chamber formation is not fully understood. From our analysis of subcellular actomyosin organization in WT cardiomyocytes at 36 hpf, we found that cells in the OC exhibit less F-actin in their lateral and apical membranes compared to IC

cells, as well as greater proportions of F-actin in basal membranes compared to IC cells. Additionally, levels of p-Myo in apical membranes are greater in IC cells than OC cells. These observations build on prior knowledge in the field about subcellular actomyosin organization in the developing curvatures by evaluating subcellular actomyosin from slices through a three-dimensional view each cell, revealing actomyosin in basal, apical, and lateral membranes as opposed to other studies where actomyosin organization has been evaluated from a two-dimensional, top-down perspective of apical cell surfaces (Itasaki et al., 1989; Deacon et al., 2010). These approaches tend to describe F-actin as primarily "cortical" in IC cells (i.e. F-actin appears most enriched around the lateral cell boundaries), and both "cortical" and "cytoplasmic" F-actin in OC cells (i.e. F-actin bundles can be seen crossing between the lateral cell boundaries). While these descriptions are valuable, our three-dimensional analysis adds new layers of understanding to this model of F-actin organization. For example, we posit that "cortical" F-actin represents F-actin associated with the lateral membranes, whereas "cytoplasmic" F-actin represents F-actin associated with the basal and apical membranes. Understanding the precise subcellular landscape of actomyosin is of particular interest, as cytoskeletal localization can help us predict its function(s) (Heisenberg & Bellaïche, 2013; Merks et al., 2018). We were therefore intrigued to observe that cells in the OC exhibit decreased localization of actomyosin in their apical membranes and increased localization of basal F-actin compared to cells in the IC, as actomyosin-based tissue tension along the apicobasal axis has been shown to be involved in mediating tissue tension during cardiac morphogenesis (Merks et al., 2018). Additionally, studies in multiple organisms have demonstrated that apical constriction mediated by F-actin contractility can be a powerful driver of tissue morphogenesis (Sawyer et al., 2010). Therefore, given the observation that IC cells exhibit a greater localization of apical actomyosin than OC

cells, we suspect that apical constriction could be an important underlying mechanism for the development of differential OC and IC cell morphologies. Similarly, it is interesting to think about how IC cells exhibit increased levels of F-actin in their lateral membranes compared to OC cells, as actomyosin in lateral membranes influences cell-cell tension and cohesion by interacting with adhesion complexes (Guillot & Lecuit, 2013). Integrating our observations of subcellular actomyosin organization with what is known about actomyosin activities in each membrane, one could imagine a situation where increased levels of lateral or "cortical" F-actin in IC cells contribute to increased intercellular surface tension, thereby preventing cell elongation in the planar axis; while the comparably lower levels of lateral F-actin in OC cells enable them to extend in this way (Lecuit, T. & Lenne, PF., 2007). Moreover, increased basal F-actin in OC cells could be stabilizing connections with the plasma membrane (Lecuit, T. & Lenne, PF., 2007), thereby preventing the apicobasal cell expansion seen in IC cells. These proposed examples would explain the cell morphology changes between OC and IC cardiomyocytes observed in preliminary studies from our group (Figure 1, Figure 2; Leerberg, unpublished). In thinking about how curvature-specific differences in actomyosin organization may be influencing the acquisition of regionalized cell morphologies, it will be important to consider the precise patterns of subcellular actomyosin organization and how the relative localization of these proteins may be influencing cell shapes in a given region.

Considering how subcellular patterns of actomyosin organization are regulated and contribute to curvature-specific morphologies, we chose to investigate *tbx5a* mutants based on preliminary evidence from our group that demonstrated how *tbx5a* mutants fail to develop the curvature-specific differences in cell morphologies that are seen in WT cells by 50 hpf (Figure 2; Leerberg, unpublished). Our findings demonstrate that *tbx5a* mutants indeed fail to develop the

same curvature-specific differences in actomyosin organization that are seen in WT cells at 36 hpf. Specifically, we find that *tbx5a* mutants lose the basal and apical F-actin curvature differentials seen in WT, as well as the apical p-Myo curvature differential. As previously mentioned, apical actomyosin has been shown to be important for mediating apical constriction of cells (Sawyer et al., 2010), so it is possible that the aberrant increase of apical actomyosin in *tbx5a* OC cells relative to WT cells is leading to apical constriction and thus preventing these cells from elongating and expanding their apical surface areas. Alternatively, it has also been demonstrated that chamber formation is driven by actomyosin tension along the apicobasal axis (Merks et al, 2018); perhaps the disrupted organization of actomyosin along at both the basal and apical membranes in in *tbx5a* mutants prevents this tension from being generated and thus, *tbx5a* mutants fail to undergo proper curvature formation. Synthesizing these possibilities with our actomyosin organization data and the cell morphological defects observed in 50 hpf *tbx5a* mutants, we propose that a Tbx5a pathway regulates regional patterns of actomyosin organization, which in turn drives curvature-specific cell shapes.

To determine how regional patterns of subcellular actomyosin organization emerge over time, we extended our analysis to include 30 hpf hearts. Here we find that some curvature differentials, for example that of both lateral and apical populations of F-actin, become apparent between 30 and 36 hpf. Other differentials, however, are already apparent at 30 hpf, suggesting that we will need to evaluate actomyosin organization at an earlier developmental stage to fully grasp how the actomyosin cytoskeleton is constructed (and/or reconstructed) in OC and IC cells. Additionally, although it is also possible that these curvature-specific differences in actomyosin organization already exist at the genesis of the LHT, this seems unlikely from our cursory examinations of LHT F-actin.

tbx5a mutants fail to undergo proper curvature formation (Figure 2), resulting in chamber curvatures that more closely resemble WT hearts from an earlier developmental stage. We were therefore intrigued by our observation that 30 hpf WT actomyosin organization patterns closely resemble the actomyosin organization seen in *tbx5a* mutant cells at 36 hpf. Together, these data connect the failure to develop differential patterns of regional actomyosin organization prior to 36 hpf and the failure to subsequently develop curvature-specific cell morphologies. This observation also strengthens our desire to explore the genesis of differential actomyosin organization patterns between curvatures, as well as to compare that to the timeline of *tbx5a* mutant cytoskeletal development.

Our observation that cells in proximal and distal regions of the curvatures exhibit significantly different actomyosin organizations adds yet another exciting layer to our analysis. For example, in WT cells at 30 and 36 hpf we find that basal F-actin is greater in proximal OC cells compared to distal OC cells, whereas the proportions of basal F-actin are similar between proximal and distal IC cells. Additionally, we observed the differential F-actin levels between proximal and distal OC cells is eliminated in *tbx5a* mutants. Overall, from this data we observed several differences between proximal and distal levels of F-actin in apical and basal membranes, and we see that all of these differentials are either absent or noticeably reduced in *tbx5a* mutants. Our observations from this data highlight the importance of considering trends in actomyosin organization that may be developing within the broad regions we have classified as the OC and IC, so we will continue to analyze data through this lens in the future.

In future studies investigating subcellular organization of the actomyosin network, an important next step would be to evaluate the actomyosin network in *tbx5a* mutants at 30 hpf. These data could help inform our hypothesis regarding the *tbx5a* mutant phenotype resembling a

stunted stage of WT development and provide further support for the necessity of Tbx5a in regulating the acquisition of curvature-specific patterns of actomyosin organization. Additionally, investigating the actomyosin network in earlier stages of WT hearts (e.g., 27 hpf) will help us to understand the genesis of regional differences in actomyosin organization. Furthermore, identifying the stage of development when regional differences in actomyosin organization do not yet exist would allow us to concentrate on this time to target potential molecular regulators of actomyosin organization and/or function. Future experiments will involve single-cell RNA sequencing to compare the transcriptomes of OC and IC cardiomyocytes from both WT and *tbx5a* mutant embryos, with the goal identifying genes that Tbx5a regulates to mediate the development of curvature-specific actomyosin organization patterns. Moreover, the identification of such genes could also pave the way for functional analysis of these candidates, providing even more insight into how differential patterns of subcellular actomyosin organization are formed and how they contribute to cell morphology changes during chamber curvature formation. Overall, our ongoing and future work to shed more light on these mechanistic underpinnings of chamber curvature formation will greatly improve our understanding of normal cardiac development and, incidentally, the cellular and molecular basis of congenital heart disease.

MATERIALS AND METHODS

Zebrafish

Zebrafish (*Danio rerio)* were raised and maintained using standard protocols in accordance with the guidelines of the University of California, San Diego Institutional Animal Care and Use Committee (IACUC). Zebrafish lines were generated by breeding wild-type zebrafish with zebrafish heterozygous for the *tbx5a*^{m21} mutant allele (Garrity et al., 2002). Because *tbx5a*^{m21} homozygotes do not survive to adulthood, *tbx5a* mutant embryos were produced by breeding heterozygous *tbx5a* fish. We also utilized the transgenic line *Tg(myl7:EGFP-Hsa.HRAS)*^{s883} (D'Amico et al., 2007).

Genotyping

Fish were genotyped for *tbx5a*^{m21} by performing tail biopsies on adult animals to obtain genomic DNA. Tail clips were added to a lysis buffer solution to extract genomic DNA which was then amplified by PCR using the primers F: 5'-CCAGCTCCTACCACGAACACACC-3' and R: 5'-CATTACCTCGTGAGATCGGCTGTC-3'. PCR products were then digested by the restriction enzyme AvrII and visualized by gel electrophoresis. With this protocol homozygous wild-type animals would display one 226 bp band and heterozygotes would show bands of 226 bp and 205 bp. In some cases, genotyping for *tbx5a* was performed using High-Resolution Melting Analysis (HRMA). For this method, PCR was performed using the primers F: 5'-ATCTCAGGACCTGCTGCCTC-3' and R: 5'-GTACACACCTTTCCTCTTGATGC-3' in the presence of the DNA saturating dye LC-Green^{Plus} (BioFire Defense, catalog #BCHM-ASY-0005) in a BioRad qPCR machine (CFX96™ Optics Module). Samples were then subjected to gradually increasing temperatures at a rate of 0.2°C/5 seconds and the melting temperature (Tm)

for each sample was recorded. The resulting data set was processed by the pandas (The Pandas Development Team, pandas 1.4.2) and NumPy (Harris et al., 2020) python packages to distinguish between wild-type and heterozygous *tbx5a* gDNA. Using this HRMA protocol, heterozygous animals could be easily identified by graphing changes in fluorescence intensity and looking for the presence of two discrete 'peaks' where the fluorescence intensity drops as the WT and mutant alleles denature at different temperatures and stop emitting a fluorescent signal. WT animals produce only one peak. Homozygous mutant *tbx5a* embryos were identified based on pectoral fin bud phenotypes observable at 30 hpf (Garrity et al., 2002).

Immunostaining

tbx5a heterozygotes were mated using standard protocols to produce wild-type and *tbx5a* mutant embryos, which were fixed at various stages of development. First, embryos were gently agitated in 1% PFA for 70 minutes. After three quick washes in PBS/0.1% Tween (PBSTw), embryos were vigorously rocked in fresh 0.02% saponin (Sigma-Aldrich, catalog #S4521) for 20-30 minutes, until the yolk had dissipated. PBSTw washes were repeated, and embryos were incubated in 4% PFA for at least 4 hours at room temperature or overnight at 4°C. After brief washes in PBSTw, 1 ml of acetone chilled at -20°C was added to embryos and samples were stored at -20°C for 8 minutes. The acetone was then aspirated off and 1 ml of PBS (1X) + Triton (0.5%) was added to embryos while hearts were dissected manually and placed into a 9 well glass dish. Hearts were incubated in a block solution containing goat serum and bovine serum for 1 hour. Embryos were incubated overnight at 4°C in primary antibodies diluted in blocking solution. The following primary antibodies were used in our experiments and at the following concentrations: chicken-anti-GFP (Thermo Fisher Scientific, catalog #A10262) [1:1000], rabbit-anti-phospho-Myosin (abcam, catalog #ab2480) [1:100], mouse-anti-Alcama (Developmental

Studies Hybridoma Bank, clone Zn-5) [1:50]. After five 10-minute washes in PBSTw on a hula shaker, embryos were again incubated in a blocking solution for 1 hour. Embryos were incubated in secondary antibodies diluted 1:300 overnight at 4℃. The secondary antibodies used in our experiments were: goat-anti-mouse-647 (Thermo Fisher Scientific, catalog #A21237), goat-anti-rabbit-647 (Thermo Fisher Scientific, catalog #21245), goat-anti-rabbit-546 (Thermo Fisher Scientific, catalog #A11010), goat-anti-chicken-488 (Thermo Fisher Scientific, catalog #A11039). Phalloidin-488 (Thermo Fisher Scientific, catalog #A12379) or Phalloidin-Rhodamine (Thermo Fisher Scientific, catalog #R415) were added at 1:30 concentrations to secondary antibody solutions to stain for filamentous actin. After washing in PBSTw, hearts were mounted and imaged with a Leica SP8 confocal laser scanning microscope. Z-stack slices were collected every 0.3 μm and then exported for 3D rendering in Imaris (Bitplane).

Image Analysis

Partitioning of the Ventricle

Z-stack slices collected by confocal microscopy were exported to Imaris (Bitplane) for three-dimensional rendering and analysis. Boundaries of the ventricle were determined based on morphological traits of the atrioventricular canal (AVC) and the outflow tract (OFT). The oblique slicer function was used to mark distinct regions of the heart and within each curvature. Regions were identified using previously described morphometric markers (Auman et al., 2007).

Generation of Single Cell Images

For subcellular analysis of F-actin and p-Myo, immunostaining and confocal imaging were performed as described above. To capture snapshots of individual cells on Imaris, one (Figure 3) or two (Figure 4, Figure 5) 1.42 μm oblique slicers were positioned to bisect a single

cell. For the data shown in Figure 3, one slicer was positioned in the center of a cell to capture snapshots in an arbitrary X axis. For the data shown in Figure 4 and Figure 5, we utilized two slicers positioned perpendicular to each other so that we could capture snapshots of each cell in its X and Y axes, where X and Y are perpendicular, lateral axes, and Z is the apicobasal axis. The volume of the image was removed, leaving two perpendicular 1.42 μm thick partial reconstructions. Snapshots were collected for each X and Y slicer showing each fluorescent channel and were then imported into Fiji to collect information about the apicobasal distribution of F-actin and p-Myo.

Quantification of Fluorescent Intensities

Information about fluorescent intensities was collected using Fiji. For the experiments shown in Figure 3, we drew straight lines with a width of 75 pixels from the cell's basal membrane to the apical membrane in the middle of the cell. The pixel intensities of the F-actin and p-Myo channels were captured along this line spanning the basal-to-apical axis, providing a readout of apicobasal F-actin and p-Myosin distribution. For experiments described in Figure 4, we sought to collect mean fluorescence signal intensities of Phalloidin and p-Myo for each cell membrane (i.e., every snapshot would contain one basal membrane, one apical membrane, and two lateral membranes; see Figure 4). Membrane boundaries were identified by the membrane bound Ras-EGFP signal of *Tg(myl7:EGFP-Hsa.HRAS)*^{s883} (D'Amico et al., 2007). First, we drew a four-sided polygon, such that the corners of the polygon reside at the boundaries between each membrane (e.g, where a lateral membrane and the apical membrane meet). We then placed 1.25 μm squares at the four vertices of the polygon to denote the boundaries of each membrane. Freehand lines with a thickness of 75 pixels were then drawn along the apical, basal, and lateral membranes of each cell; to avoid unintentionally including signal from adjacent membranes, we

excluded signal within the corner squares when drawing freehand lines. We then measured the mean signal intensity throughout the region captured by each line for the F-actin and p-Myo fluorescence channels. The data generated here were processed and visualized by scripts written in R. For the images shown in Figures 3-5, representative images were chosen that represented the typical phenotypes observed for that condition.

Detection of Outliers

Due to experimental variance in the levels of fluorescence intensity produced by immunostaining, we developed a method to identify 'outlier' samples with fluorescence values that fell outside of the typical ranges of values observed. Before capturing individual cell snapshots, we utilized the surfaces tool in Imaris to encompass the cardiomyocyte layer of the ventricle and to determine the mean fluorescence signal intensity of F-actin and p-Myo within this region. The data were exported to R and then subjected to statistical analysis to identify outlying samples. Outliers were excluded from subsequent analysis.

Statistics and Plotting

Statistical analysis was performed in R and RStudio, using standard packages (R Core Team, 2015) and scales (Wickham, 2022). To test for significant differences between groups, Wilcoxon tests were performed using a confidence interval of 0.05. P values less than 0.05 were considered as statistically significant. Biological replicates (n) were defined as the total number of individual hearts analyzed or the number of cells analyzed in experiments where subcellular data were measured and are reported in figure legends. Plots were produced in R and RStudio using tidyr (Wickham & Girlich, 2022), dplyr (Wickham et al., 2022), scales (Wickham & Seidel, 2022), ggplot2 (Wickham, 2016) and ggBeeswarm (Clarke & Sherrill-Mix, 2017).

REFERENCES

Auman, H. J., Coleman, H., Riley, H. E., Olale, F., Tsai, H.-J., & Yelon, D. (2007). Functional Modulation of Cardiac Form through Regionally Confined Cell Shape Changes. *PLOS Biology*, 5(3), e53.

Bakkers, J. (2011). Zebrafish as a model to study cardiac development and human cardiac disease. *Cardiovascular Research*, 91(2), 279.

Bartman, T., & Hove, J. (2005). Mechanics and function in heart morphogenesis. *Developmental Dynamics*, 233(2), 373–381.

Bruneau, B. G., Nemer, G., Schmitt, J. P., Charron, F., Robitaille, L., Caron, S., Conner, D. A., Gessler, M., Nemer, M., Seidman, C. E., & Seidman, J. G. (2001). A Murine Model of Holt-Oram Syndrome Defines Roles of the T-Box Transcription Factor Tbx5 in Cardiogenesis and Disease. *Cell*, 106(6), 709–721.

Buckingham, M., Meilhac, S., & Zaffran, S. (2005). Building the mammalian heart from two sources of myocardial cells. *Nature Reviews Genetics*, 6(11), 826–835.

Charlène, G. & Thomas, L. (2013). Mechanics of Epithelial Tissue Homeostasis and Morphogenesis. *Science*, *340*(6137), 1185–1189.

Christoffels, V. M., Burch, J. B. E., & Moorman, A. F. M. (2004). Architectural Plan for the Heart: Early Patterning and Delineation of the Chambers and the Nodes. *Trends in Cardiovascular Medicine*, 14(8), 301–307.

Christoffels, V. M., Habets, P. E. M. H., Franco, D., Campione, M., Jong, F. de, Lamers, W. H., Bao, Z.-Z., Palmer, S., Biben, C., Harvey, R. P., & Moorman, A. F. M. (2000). Chamber Formation and Morphogenesis in the Developing Mammalian Heart. *Developmental Biology*, 223(2), 266–278.

Clark, A. G., Dierkes, K., & Paluch, E. K. (2013). Monitoring Actin Cortex Thickness in Live Cells. *Biophysical Journal*, *105*(3), 570–580.

Clarke, E., & Sherrill-Mix, S. (2017). *Ggbeeswarm: Categorical Scatter (Violin Point) Plots*. https://CRAN.R-project.org/package=ggbeeswarm.

D'Amico, L., Scott, I. C., Jungblut, B., & Stainier, D. Y. R. (2007). A Mutation in Zebrafish hmgcr1b Reveals a Role for Isoprenoids in Vertebrate Heart-Tube Formation. *Current Biology*, 17(3), 252–259.

Deacon, D. C., Nevis, K. R., Cashman, T. J., Zhou, Y., Zhao, L., Washko, D., Guner-Ataman, B., Burns, C. G., & Burns, C. E. (2010). The miR-143-adducin3 pathway is essential for cardiac chamber morphogenesis. *Development*, 137(11), 1887–1896.

de Pater, E., Clijsters, L., Marques, S. R., Lin, Y.-F., Garavito-Aguilar, Z. V., Yelon, D., & Bakkers, J. (2009). Distinct phases of cardiomyocyte differentiation regulate growth of the zebrafish heart. *Development*, 136(10), 1633–1641.

Eder, D., Aegerter, C., & Basler, K. (2017). Forces controlling organ growth and size. *Roles of Physical Forces in Development*, 144, 53–61.

García-Castro Martín I., Vielmetter Eva, & Bronner-Fraser Marianne. (2000). N-Cadherin, a Cell Adhesion Molecule Involved in Establishment of Embryonic Left-Right Asymmetry. *Science*, 288(5468), 1047–1051.

Garrity, D. M., Childs, S., & Fishman, M. C. (2002). The heartstrings mutation in zebrafish causes heart/fin Tbx5 deficiency syndrome. *Development*, *129*(19), 4635–4645.

Greulich, F., Rudat, C., & Kispert, A. (2011). Mechanisms of T-box gene function in the developing heart. *Cardiovascular Research*, 91(2), 212–222.

Guillot Charlène & Lecuit Thomas. (2013). Mechanics of Epithelial Tissue Homeostasis and Morphogenesis. *Science*, *340*(6137), 1185–1189.

Harris, C. R., Millman, K. J., van der Walt, S. J., Gommers, R., Virtanen, P., Cournapeau, D., Wieser, E., Taylor, J., Berg, S., Smith, N. J., Kern, R., Picus, M., Hoyer, S., van Kerkwijk, M. H., Brett, M., Haldane, A., del Río, J. F., Wiebe, M., Peterson, P., … Oliphant, T. E. (2020). Array programming with NumPy. *Nature*, 585(7825), 357–362.

Heisenberg, C.-P., & Bellaïche, Y. (2013). Forces in Tissue Morphogenesis and Patterning. *Cell*, 153(5), 948–962.

Itasaki, N., Nakamura, H., & Yasuda, M. (1989). Changes in the arrangement of actin bundles during heart looping in the chick embryo. *Anatomy and Embryology*, 180(5), 413–420.

Latacha, K. S., Rémond, M. C., Ramasubramanian, A., Chen, A. Y., Elson, E. L., & Taber, L. A. (2005). Role of actin polymerization in bending of the early heart tube. *Developmental Dynamics*, 233(4), 1272–1286.

Lecuit, T., & Lenne, P.-F. (2007). Cell surface mechanics and the control of cell shape, tissue patterns and morphogenesis. *Nature Reviews Molecular Cell Biology*, *8*(8), 633–644.

Manasek, F. J., Burnside, M. B., & Waterman, R. E. (1972). Myocardial cell shape change as a mechanism of embryonic heart looping. *Developmental Biology*, 29(4), 349–371.

Männer, J. (2000). Cardiac looping in the chick embryo: A morphological review with special reference to terminological and biomechanical aspects of the looping process. *The Anatomical Record*, 259(3), 248–262.

Meilhac, S. M., Esner, M., Kerszberg, M., Moss, J. E., & Buckingham, M. E. (2004). Oriented clonal cell growth in the developing mouse myocardium underlies cardiac morphogenesis. *Journal of Cell Biology*, 164(1), 97–109.

Merks, A. M., Swinarski, M., Meyer, A. M., Müller, N. V., Özcan, I., Donat, S., Burger, A., Gilbert, S., Mosimann, C., Abdelilah-Seyfried, S., & Panáková, D. (2018). Planar cell polarity signalling coordinates heart tube remodelling through tissue-scale polarisation of actomyosin activity. *Nature Communications*, 9(1), 2161.

Moorman, A. F. M., & Christoffels, V. M. (2003). Cardiac Chamber Formation: Development, Genes, and Evolution. *Physiological Reviews*, 83(4), 1223–1267.

Munjal, A., & Lecuit, T. (2014). Actomyosin networks and tissue morphogenesis. *Development*, 141(9), 1789–1793.

Noël, E. S., Verhoeven, M., Lagendijk, A. K., Tessadori, F., Smith, K., Choorapoikayil, S., den Hertog, J., & Bakkers, J. (2013). A Nodal-independent and tissue-intrinsic mechanism controls heart-looping chirality. *Nature Communications*, 4(1), 2754.

Plageman Jr, T. F., & Yutzey, K. E. (2005). T-box genes and heart development: Putting the "T" in heart. *Developmental Dynamics*, 232(1), 11–20.

R Development Core Team (2015) R: A Language and Environment for Statistical Computing. R Foundation for Statistical Computing, Vienna.

Sawyer, J. M., Harrell, J. R., Shemer, G., Sullivan-Brown, J., Roh-Johnson, M., & Goldstein, B. (2010). Apical constriction: A cell shape change that can drive morphogenesis. *Special Section: Morphogenesis*, 341(1), 5–19.

Shiraishi, I., Takamatsu, T., Minamikawa, T., & Fujita, S. (1992). 3-D observation of actin filaments during cardiac myofibrinogenesis in chick embryo using a confocal laser scanning microscope. *Anatomy and Embryology*, 185(4), 401–408.

Sidhwani, P., & Yelon, D. (2019). Chapter Eleven—Fluid forces shape the embryonic heart: Insights from zebrafish. In D. M. Wellik (Ed.), *Current Topics in Developmental Biology* (Vol. 132, pp. 395–416). Academic Press.

Singh, J., & Mlodzik, M. (2012). Planar cell polarity signaling: Coordination of cellular orientation across tissues. *WIREs Developmental Biology*, 1(4), 479–499.

Soufan, A. T., van den Berg, G., Ruijter, J. M., de Boer, P. A. J., van den Hoff, M. J. B., & Moorman, A. F. M. (2006). Regionalized Sequence of Myocardial Cell Growth and Proliferation Characterizes Early Chamber Formation. *Circulation Research*, 99(5), 545–552.

Srivastava, D. (2006). Making or Breaking the Heart: From Lineage Determination to Morphogenesis. *Cell*, 126(6), 1037–1048.

Stalsberg, H. (1969). Regional mitotic activity in the precardiac mesoderm and differentiating heart tube in the chick embryo. *Developmental Biology*, 20(1), 18–45.

Stalsberg, H. (1970). Mechanism of dextral looping of the embryonic heart. *Development and Ultrastructure of the Embryonic Heart. Part Two*, *25*(3), 265–271.

Taber, Larry A. (2006). Biophysical mechanisms of cardiac looping. *Int. J. Dev. Biol.*, 50, 323–332.

Tessadori, F., Tsingos, E., Colizzi, E. S., Kruse, F., van den Brink, S. C., van den Boogaard, M., Christoffels, V. M., Merks, R. M., & Bakkers, J. (2021). Twisting of the zebrafish heart tube during cardiac looping is a tbx5-dependent and tissue-intrinsic process. *ELife*, 10, e61733.

The Pandas Development Team (2020). Pandas, *Zenodo*, 1.0.3. https://doi.org/10.5281/zenodo.3509134.

Thompson, R. P., Lindroth, J. R., & Wong, Y. M. (1990). Regional differences in DNA-synthetic activity in the preseptation myocardium of the chick. *Developmental Cardiology: Morphogenesis and Function*. 219–234.

Voronov, D. A., Alford, P. W., Xu, G., & Taber, L. A. (2004). The role of mechanical forces in dextral rotation during cardiac looping in the chick embryo. *Developmental Biology*, 272(2), 339–350.

Wickham, H., François, R., Henry, L., Müller, K. (2022). *dplyr: A Grammar of Data Manipulation*. https://dplyr.tidyverse.org, https://github.com/tidyverse/dplyr.

Wickham, H. & Girlich, M. (2022). *tidyr: Tidy Messy Data*. https://tidyr.tidyverse.org, https://github.com/tidyverse/tidyr.

Wickham, H. & Seidel, D. (2022). *scales: Scale Functions for Visualization*. https://scales.r-lib.org, https://github.com/r-lib/scales.

Wickham, H. (2016). *ggplot2: Elegant Graphics for Data Analysis.* Springer, 147–168.

ACKNOWLEDGEMENTS

Figure 1 contains material adapted from Auman et al., 2007 as well as unpublished work by Dena M. Leerberg. Figure 2 contains unpublished material coauthored with Dena M. Leerberg.